11th International Conference on Power Electronics-ECCE Asia
May 22 - 25, 2023 / ICC Jeju, Jeju, Korea

Optimizing Current-Fed, GaN-Based DC-DC Converters for Electrolysis Applications

Niklas Fritz, Tudor Sechel, Paul Kowalewski, and Rik W. De Doncker
Institute for Power Electronics and Electrical Drives
RWTH Aachen University, Germany
post@isea.rwth-aachen.de

***Abstract*—The market for proton exchange membrane (PEM) electrolyzers is expected to grow substantially in the coming years, following an increasing demand for green hydrogen. Power electronics is a key enabling technology for supplying future PEM electrolyzers, however the literature addressing power-electronic converters for electrolysis applications is still quite limited. This paper addresses a dc-dc converter for a 10 kW PEM electrolyzer using gallium nitride (GaN) semiconductor devices and performs a multi-objective optimization for efficiency and power density. In contrast to previous work, a very wide topology family is considered. From the results, critical design decisions are deduced. Moreover, the same genetic algorithm is used to identify efficiency-optimized modulation strategies. The gained insights significantly broaden the scope of suitable dc-dc converter topologies for electrolysis applications.**

***Index Terms*—Green hydrogen, dc-dc converter, multi-objective optimization, current-fed converter, gallium nitride**

I. Introduction

Green hydrogen will play a key role in future utility grids and the stability of the electric energy supply. Proton exchange membrane (PEM) electrolyzers are addressed both by research and industry to increase the efficiency and reduce the cost of hydrogen generation. Also from the perspective of power electronics, PEM electrolyzers present challenges, as usually the stack voltage does not exceed a few 100 V, thus requiring high current ratings, while the ripple components of the current have to be minimized. Expecting a substantial market growth for PEM electrolyzers, power-electronic engineers have to provide high-power, efficient, reliable, scalable, and affordable converter architectures. Multi-objective optimization [1], [2] as well as design automation [3] could be useful tools to address these goals. Moreover, wide-bandgap (WBG) semiconductor devices based on silicon carbide (SiC) or gallium nitride (GaN) have the potential to realize high efficiencies, while maintaining low current ripple amplitudes [4], [5].

As already stated, PEM electrolyzers, similar to fuel cells, are sensitive to ripple currents. Literature [6]–[9] shows that while the hydrogen production rate is determined by the dc component of the current, the losses are dependent on the rms value, which implies that lower ripple amplitudes increase the efficiency of the electrolysis. However, [6]–[9] assume unrealistically large ripple amplitudes by omitting filter components in the power-electronic converters. In [10], a more realistic scenario with ripple amplitudes below 10 % of the dc current reveals efficiencies comparable to a pure dc current. However, it has also been shown that ripple currents degrade the lifetime of an electrolysis cell. In [11], it is shown that a dc current with a superimposed 10 kHz triangular ripple current of 10 % amplitude massively accelerated the aging of the PEM electrolysis cell compared to the aging caused by a pure dc current. Similar studies have been published for fuel cells [12], [13]. Therefore, until the impacts of ripple currents on electrolyzers are fully clarified, the projected converter aims for a rigorous minimization of the ripple amplitude.

While for large-scale multi-megawatt electrolyzers, thyristor-based topologies are still the state of the art, multiple power-electronic topologies have been discussed for electrolyzers with lower power ratings. This paper focuses on a dc-dc converter supplying a PEM electrolyzer from a dc rail. The literature on such dc-dc converters in the multi-kilowatt range is limited, but mainly proposes isolated resonant [14], [15] or isolated dual-active bridge (DAB) [16]–[18] converters for electrolyzer (or fuel cell) applications. A particularly interesting converter family are current-fed converters, as they massively reduce ripple currents [19]–[21].

This paper explores a much wider range of topologies for a 400 V to 50 V, GaN-based dc-dc converter rated 10 kW to supply a PEM electrolyzer with minimal ripple current. A genetic algorithm, an efficient tool in multi-objective converter optimization [5], [22], is used to optimize the converter family for minimum losses and size. From the results, critical design decisions are deduced, such as the choice of topology, the optimal degree of modularity, the transformer design, and many more. Moreover, the same genetic algorithm is used to identify efficiency-optimized modulation strategies. The gained insights significantly broaden the scope of suitable dc-dc converter topologies for electrolysis applications.

Section II introduces the topology family and section III discusses the optimization technique. The optimization results are presented in section IV, followed by an optimization of the associated modulation techniques in section V. Finally, section VI gives a conclusion.

II. Topology Family

The challenges of the projected dc-dc converter are the high current rating as well as the requirement for minimum ripple at the eletrolyzer output. Such challenges are also faced in fuel cell applications, as fuel cells have a similar electrical behavior, albeit with reversed current direction.

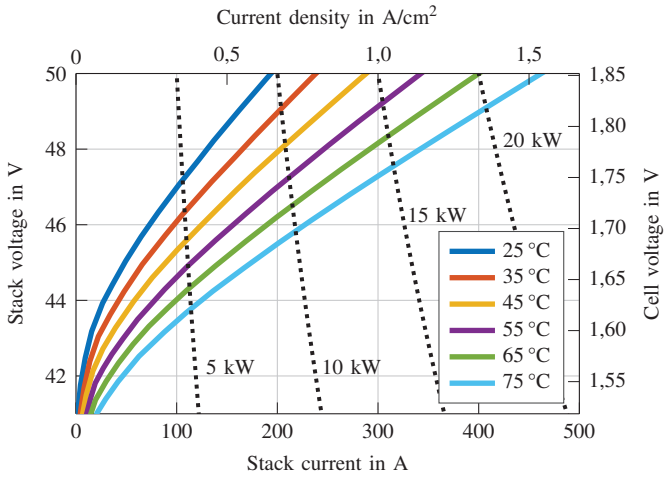

Figure 1: Temperature-dependent polarization curve and I-V-characteristic of the PEM electrolyzer in the target application [23], [24]

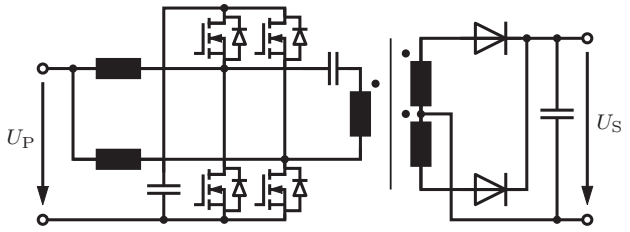

Figure 2: Schematic of the originally proposed current-fed converter [19] with a current-fed port on the primary side

Fig. 1 shows the so-called polarization curve of the PEM electrolyzer in the target application, which consists of 27 series-connected cells with an electrode area of 300 cm^2 [23], [24]. Not only are the overall stack voltage and current displayed, but also the cell-related quantities, i.e., current density and cell voltage. Moreover, the power delivery is indicated in dashed lines. The projected dc-dc converter shall be designed for a 10 kW operating point at 50 V stack voltage and 200 A stack current. The input voltage of the dc-dc converter is assumed 400 V.

A power-electronic topology that is tailored to the requirements of a fuel cell has been proposed and widely recognized in [19], Fig. 2 shows its schematic. It consists of an isolated resonant converter that is merged on the primary side with an interleaved boost converter, a so-called current-fed port, to which the fuel cell is connected. In the current-fed port, the two half bridges operate at 50 % duty cycle and 180° out of phase, such that the resulting triangular current waveforms in the two inductors are also 180° out of phase and add up to a ripple-free, constant dc current. Another advantage is that since the comprised two-phase boost converter steps up the voltage by a factor of two, twice the fuel-cell current can be realized. This way, both requirements for a high, but ripple-free current are met.

For the projected dc-dc converter, the topology in Fig. 2 is taken as a basis for a whole family of considered topology variants, which are shown in Fig. 3. Since in an electrolyzer application, the low-voltage, high-current port is the output, the topology from Fig. 2 is reversed and the current-fed circuit is connected to the secondary side. This requires actively controlled switches instead of diodes, making the topology bidirectional and hence also suitable for fuel cell or battery storage applications.

Looking at the topology variants shown in Fig. 3, different topological options are considered for the primary-side circuit, the transformer, and the secondary-side circuit. For both the primary and the secondary side, full-bridge and half-bridge configurations are considered. To maintain the current-fed property of the secondary side, using a half bridge means using two separate half-bridge circuits with dedicated transformer windings that are antiparallel. Additionally, due to the high output current of up to 200 A, the number of secondary-side circuits N_S may be greater than one as inspired by [25]–[27]. Adding resonant capacitors on the primary and/or secondary side, the topology naming also changes from the DAB (without any capacitors) to the bidirectional LLC converter (a resonant capacitor on the primary side only) or the CLLC converter (resonant capacitors on both sides), making a total of three topologies considerable for the application. For the full-bridge configuration, the resonant capacitor is placed in series with the transformer winding, whereas for the half-bridge configuration, it is split into two capacitors and used as dc-link with center tap. If no resonant capacitor is used, the two dc-link capacitors are increased in size such that they form a capacitive voltage divider. Therefore, the choice of topology is a matter of sizing the resonant capacitors. Finally, not only one lumped transformer is considered, but also a modular, so-called matrix transformer that consists of separate transformers for each secondary-side circuit. Inspired by [25], its primary-side windings can be connected in series such that the turns ratio for every transformer reduces.

From a modelling point of view, the CLLC converter is the most generic of the three topologies, because the LLC and the DAB converter can be derived from the CLLC converter by assuming sufficiently large values for the secondary-side resonant capacitance or both resonant capacitances, respectively. For the CLLC converter, multiple modulation strategies have been proposed [28]. However, the secondary-side bridges are required to operate at 50 % duty cycle and 180° out of phase to maintain the current-fed property, which limits the choice of modulation strategies. Additionally, not all modulation strategies, e.g., conventional frequency control, have multi-port capability, which is needed to ensure the power sharing among multiple secondary sides. Therefore, a single phase-shift (SPS) modulation strategy at a fixed switching frequency is assumed, because the phase-shift angle can be adapted for each secondary side individually. In SPS modulation, all switches are operated at 50 % duty cycle and the power flow is controlled by the phase-shift angle φ between the voltage patterns of the primary side and the respective secondary side, thus manipulating the voltage drop across the resonant tank [28].

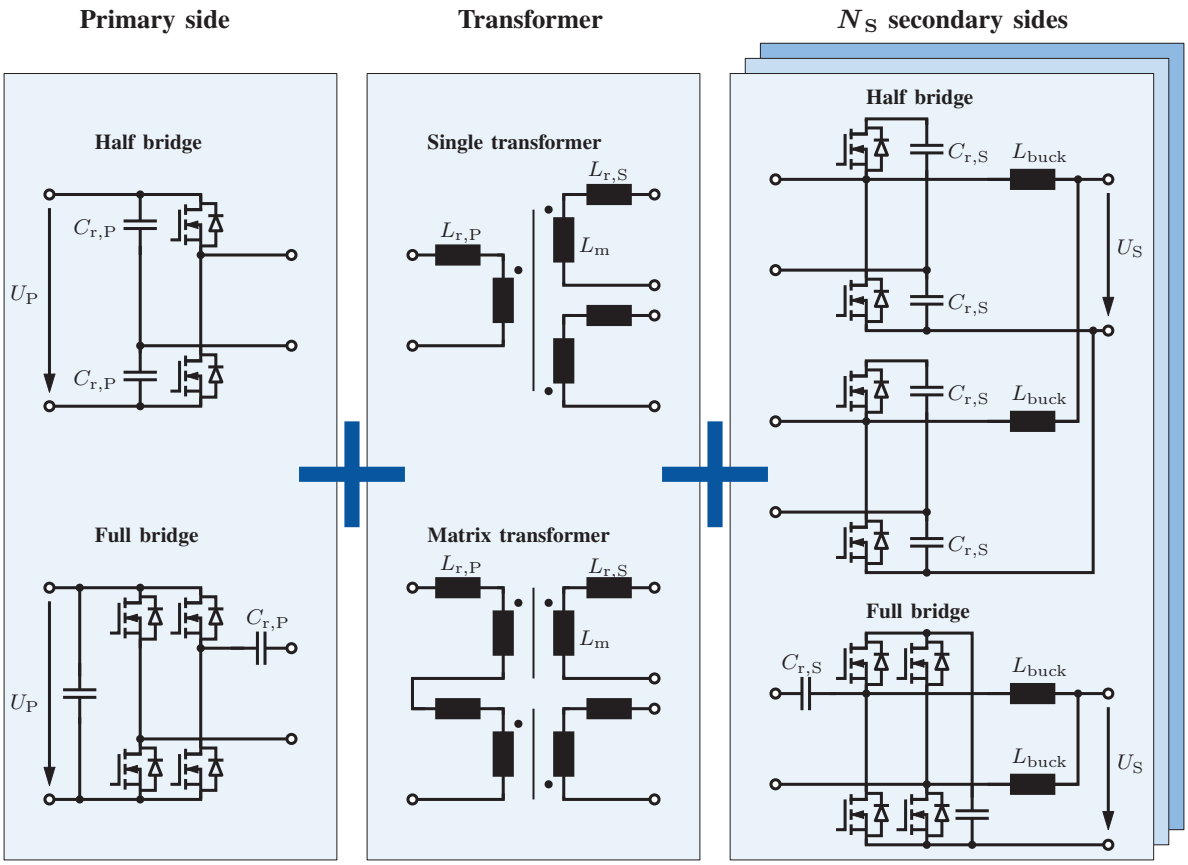

Figure 3: Overview of the considered topology variants

III. Design Optimization

This section describes the multi-objective optimization of the topology variants from Fig. 3. First, the mathematical formulation of the optimization problem and suitable solving methods are introduced, followed by a discussion of the converter model.

A. Formulating and Solving the Optimization Problem

As stated in [5], [22], [29], an optimization problem in power electronics is mathematically described as shown in (1):

$$\begin{aligned} &\min_{\vec{x}} \left\{ \vec{y} : \ \mathbb{R}^{\mathrm{n}} \times \mathbb{N}^{\mathrm{m}} \to \mathbb{R}^{\mathrm{q}}, \ \ \vec{y} = \vec{F}(\vec{x}, \vec{r}) \right\}, \\ &\text{subject to} \quad \vec{h}(\vec{x}, \vec{r}) \leq 0, \ \ \vec{g}(\vec{x}, \vec{r}) = 0, \\ &\text{and} \quad \vec{x}_{\mathrm{l}} \leq \vec{x} \leq \vec{x}_{\mathrm{u}}. \end{aligned} \tag{1}$$

The design variables $\vec{x}$ completely identify one converter design. They consist of n continuous design variables, such as the switching frequency or the size of the passive components, and m discrete variables that describe, for example, the different topology variants or the choice of a core material or a certain semiconductor device. For each design variable, it is practical to provide lower and upper boundaries, summarized by the vectors $\vec{x}_{\mathrm{l}}$ and $\vec{x}_{\mathrm{u}}$, respectively. Whereas the boundaries constrain the continuous design variables to a physically sensible range, they simply model the finite number of choices for the discrete design variables. The objective function $\vec{F}$ maps the design variables to the performance variables $\vec{y}$, such as the converter losses, its weight, size, cost, or other properties. Moreover, the requirements $\vec{r}$ contain quantities that are constant for every design, such as the operating area, defined by the input and output voltages and the power rating, or component limitations such as saturation flux densities. Finally, the equality and inequality constraints $\vec{g}$ and $\vec{h}$, respectively, mathematically express these requirements.

For the given topology family, the two considered objectives are the losses of the converter at the full-load operating point as well as its power density. As both the volumetric and the gravimetric power density rely on rather imprecise volume or weight models, an electrical quantity which correlates with power density is utilized in this paper: the overall stored energy in the resonant passive components. This quantity can be calculated very easily and comes with much less uncertainties than a loss or volume model, which is sometimes even generated by correlation with the stored energy. Hence, the considered optimization is a multi-objective optimization, because it is performed for a two-dimensional performance vector $\vec{y}$. Therefore, the results will be a set of Pareto-optimal solutions.

Table I: List of the 17 design variables identifying a converter

Design Variable	Boundaries
Switching frequency f_{sw}	100…500 kHz
Normalized resonant frequency $f_{\mathrm{s}}/f_{\mathrm{sw}}$	0.1…0.9
Transformer leakage reactance X_{s}	0.637…10.93 Ω
Transformer magnetizing reactance X_{m}	63.7…1093 Ω
Buck inductor reactance X_{buck}	0.314…314 Ω
Number of secondary sides N_{S}	1, 2 and 4
Primary-side configuration	full bridge or half bridge
Secondary-side configuration	full bridge or half bridge
Topology	DAB, LLC, or CLLC
Transformer configuration	single or matrix
Primary-side semiconductor device	GS66516T, IGOT60R070D1
Secondary-side semiconductor device	the above and EPC2034C
Selection of magnetic core	18 ELP cores as in [30]
Magnetic material, transformer core	3C95, 3C96, 3C98,
Magnetic material, buck inductors	N87, N49, PC200
Number of parallel transformer cores	1…5
Number of parallel inductor cores	1…5

The overall time required for the optimization depends on the computation time required for a single evaluation of the objective function and the overall number of evaluations required to find the solution [22]. Metaheuristic algorithms, such as genetic algorithms, have proven to be very effective in reducing the overall number of evaluations of the objective function [5]. In genetic optimization, a so-called generation of, in this case, 150 designs is randomly generated and evaluated, obtaining the full-load losses and the stored energy. According to the principle of the "survival of the fittest", the best designs will generate the next generation under certain stochastic variations. This process is repeated until the set of Pareto-optimal designs in each generation, the Pareto front, converges. To save computation time, the designs in one generation are evaluated simultaneously on a multi-core computer.

A total of 17 design variables are defined to fully describe one converter design, listed in Table I. The 17 variables consist of 5 continuous design variables: the switching frequency f_{sw}, the normalized resonant frequency, and the reactances of the transformer and the buck inductors. It must be ensured that the design variables are not cross-coupled, e.g., that a change in the switching frequency neither affects the other design variables nor changes the electrical behavior of the converter. Therefore, reactances instead of inductances are used, and the resonant frequency is normalized to the switching frequency. The resonant capacitances are calculated from the normalized resonant frequency. Additionally, 12 discrete design variables are implemented, which describe the topology variants from section II, the choice of GaN transistors for the primary and secondary side, and the magnetic cores used for the transformer and the inductors. Six different ferrite materials are considered, and planar transformers and inductors using the ELP core selection from [30] are assumed. Because of the high currents, a single turn is assumed for each secondary-side winding of the transformer. The number of turns on the primary side of the transformer depends on the turns ratio, which is determined by the full-bridge or half-bridge configuration on the primary and secondary sides, as well as by whether a single or a matrix transformer is used. To increase the variety of core configurations, it is also assumed that multiple ELP cores can be connected in parallel to increase the magnetic area, both for the transformer and the buck inductors individually.

A non-linear inequality constraint implements the power equation of a CLLC converter as derived in [31], ensuring that each design has a maximum power capability of at least the rated power of 10 kW at the maximum phase-shift angle of $\pi/2$. Another constraint ensures that the phase-shift angle used at the full-load operating point is larger than $\pi/6$, which is required to ensure a sufficient controllability of the converter throughout its operating range. Two additional constraints ensure that the maximum flux densities in the transformer and inductor cores both remain below 80 % of the saturation flux density of the used magnetic material.

B. Converter Modelling

Evaluating the objective function $\vec{F}$ from (1), i.e., finding the full-load losses and the peak resonant energy for a certain design $\vec{x}$, requires either analytical models as used in [5], [22], or a simulation framework, which is used in this case. The investigated topology family is simulated in PLECS Blockset, embedded into Matlab/Simulink. All variants and configurations are realized by configurable subsystems in PLECS that can be controlled by a variable which is set by Matlab, such that every possible topology variant, 72 in total, can be covered by a single, reconfigurable simulation model. This way, the optimization algorithm runs in Matlab, while the topology is simulated in PLECS. Returning the simulation results, the performance variables are calculated again in Matlab. In PLECS, a stopping criterion is implemented, which ensures that the simulation runs no longer than required and automatically stops when all initial transients have decayed. More precisely, the stopping criterion is reached if the peak value of the current in the buck inductors changes by less than 0.5 % moving from one switching period to the next.

In the analysis of the full-load converter losses, the following loss mechanisms are considered: First, the conduction and switching losses of the GaN semiconductor devices are directly obtained from the PLECS simulation using device models. Where device models were not available from the manufacturers, they were generated in SPICE simulations. The core losses in the transformer and the inductors were calculated after the simulation, using the simulation waveforms, the core dimensions, and the "coreloss2" tool developed by [32] using the Steinmetz parameters of the ferrites which were taken from the loss characteristics in the material data sheets. The losses in the resonant capacitors are also calculated after the simulation using a plate capacitor model, where the capacitance C and the resistance R are obtained by

$$C = \varepsilon \frac{A}{d} \quad \text{and} \quad R = \frac{d}{\sigma A}, \tag{2}$$

respectively, where d denotes the electrode distance, ε and σ the permittivity and conductivity of the dielectric, respectively, and A the electrode distance. Hence, the quantity

$$\tau = RC = \frac{\varepsilon}{\sigma} \tag{3}$$

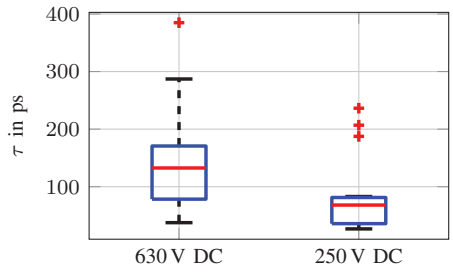

Figure 4: Technology constant τ for 630 V and 250 V dc rated capacitors

is a constant, and data of commercial ceramic capacitors with a C0G dielectric has been collected and fitted to this model, shown in Fig. 4. The worst-case parameter has been taken to calculate the capacitor losses, using 385 ps for C0G ceramic capacitors rated 630 V and 236 ps for C0G ceramic capacitors rated 250 V. Finally, the losses in the transformer and inductor windings are calculated using the simulated waveforms and the resistance of one turn, which is calculated using the average length of one turn for the selected core size and a maximum current density of 7 A/mm^2. For the selected range of switching frequencies, it is assumed that sufficiently thin conductors are used to neglect the influence of the skin effect.

The second objective, representing power density, is the total energy stored in the resonant components, such as the primary-side and secondary-side capacitors and leakage inductances of the transformers, the magnetizing inductance, and the buck inductors. For inductors, the peak energy is calculated using the peak value of the simulated inductor current waveform, since in the transformer, the average current is zero. For capacitors, the peak energy is calculated using the peak-to-peak value of the simulated capacitor voltage waveform.

IV. Results

This section discusses the optimization results and the design considerations that can be deduced.

First, an unconstrained optimization is performed, i.e., none of the design variables are restricted to a fixed value. Fig. 5 shows the Pareto fronts during the optimization process. It can be seen that after each generation, the Pareto fronts move outward until they converge.

Fig. 6 plots the continuous design variables that correspond to the final, outermost Pareto front in Fig. 5, yielding the Pareto-optimal designs. The use of GaN transistors results in high switching frequencies of several 100 kHz. Additionally, the Pareto-optimal designs are resonant converters that operate above the resonant frequency. The buck inductors are chosen small for high power densities, i.e., low stored energy, which however leads to increased losses due to the high peak currents. Therefore, the value of the reactance X_{buck} increases toward higher efficiencies. However, also the transformer reactances X_{s} and X_{m} increase toward higher resonant energies, i.e., toward higher efficiencies, together with the normalized switching frequency. This leads to a reduced

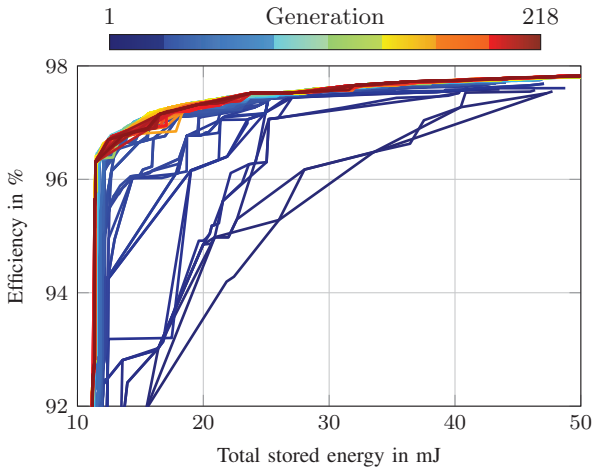

Figure 5: Evolution of the Pareto fronts for unrestricted genetic optimization

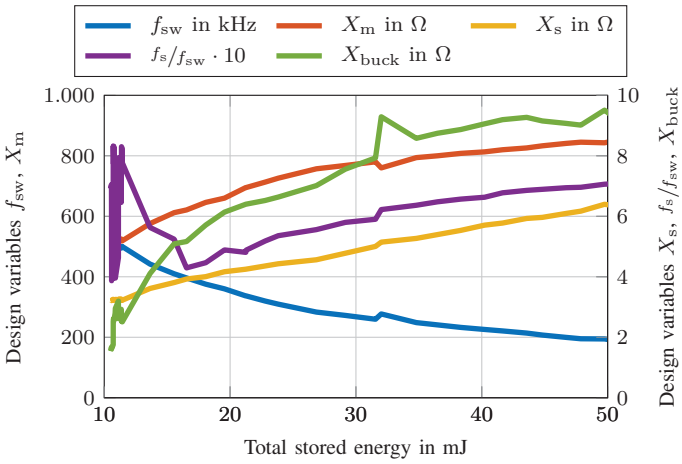

Figure 6: Pareto-optimal, continuous design variables in the final generation

harmonic content in the transformer current, resulting in lower core and high-frequency losses. A more sinusoidal shape of the current waveform also results in lower rms values, i.e., lower conduction losses, but increased peak current, leading to a higher amount of stored energy in the stray inductances.

The discrete design variables that are not shown in Fig. 6 are yet to be analyzed. For this purpose, further optimizations are performed that restrict one design variable to a fixed value. Fig. 7, for example, shows the final Pareto fronts for three optimizations that consider either only DAB, only LLC, or only CLLC converters. The difference between the three topologies is minimal, but resonant converters have slight advantages. As discussed, depending on the value of the normalized resonant frequency $f_{\mathrm{s}}/f_{\mathrm{sw}}$, the shape of the transformer current waveform changes, which can lead to lower rms current values, reducing the conduction losses, while the lower harmonic content is beneficial for lowering the core losses and the high-frequency losses.

In Fig. 8, the full-bridge and half-bridge configurations are compared. Obviously, a full bridge is advantageous on the primary side: In a full bridge, the current in the resonant

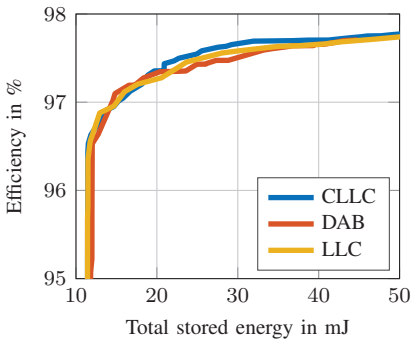

Figure 7: Effect of different converter topologies on the Pareto front

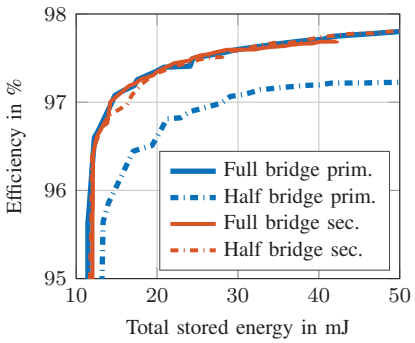

Figure 8: Effect of different primary-side and secondary-side configurations on the Pareto front

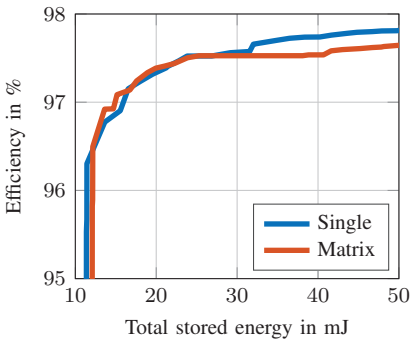

Figure 9: Effect of different transformer configurations on the Pareto front

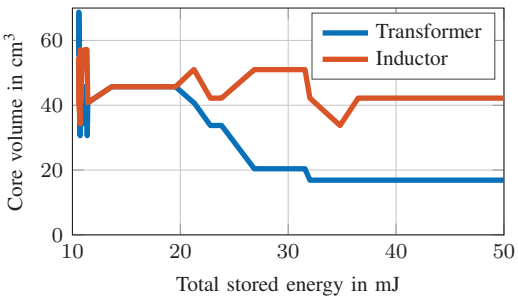

Figure 10: Pareto-optimal volumes of the core configurations

tank is reduced by a factor of two in comparison with the current that is seen with a half bridge. However, the number of semiconductor devices is doubled, leading to conduction losses that are cut in half. For the secondary side, this advantage is not observed, because two half-bridge configurations are implemented to maintain the current-fed property. This way, twice the number of semiconductor devices are used and the conduction losses are equal to those observed in the full-bridge configuration.

All Pareto-optimal designs use the device GS66516T for the primary side and the device EPC2034C for the secondary side, since they have the lowest on-state resistances. For switching frequencies up to 250 kHz, the magnetic materials 3C95 and 3C98 dominate in the selection of the transformer and the inductor cores, while the ferrite core materials N49 and PC200 are selected for frequencies above 250 kHz.

Finally, the transformer configuration is analyzed in Fig. 9. To achieve high efficiencies, a single transformer is preferable due to the lower amount of magnetic cores, and hence, lower core losses, but for power-dense converters, both options are equally attractive. Fig. 10 plots the volume of the cores, including the parallel connection. While for the transformer, the amount of magnetic material is reduced toward higher efficiencies, this cannot be achieved for the inductors due to the constant dc offset in the indcutor current.

All in all, the presented optimization framework proves helpful in taking suitable and valid design decisions when designing dc-dc converters for electrolysis applications. Still,

Table II: Values of the 17 design variables identifying the converter for which the modulation strategies are optimized

Design Variable	**Value**
Switching frequency f_{sw}	250 kHz
Normalized resonant frequency $f_{\mathrm{s}}/f_{\mathrm{sw}}$	0.636
Transformer leakage reactance X_{s}	5.27 Ω
Transformer magnetizing reactance X_{m}	794 Ω
Buck inductor reactance X_{buck}	8.58 Ω
Number of secondary sides N_{S}	4
Primary-side configuration	full bridge
Secondary-side configuration	full bridge
Topology	CLLC
Transformer configuration	single
Primary-side semiconductor device	GS66516T
Secondary-side semiconductor device	EPC2034C
Selection of magnetic core	ELP 38/8/25 and I 38/4/25
Magnetic material, transformer core	3C95
Magnetic material, buck inductors	3C98
Number of parallel transformer cores	2
Number of parallel inductor cores	4

the decision for a specific converter design is a trade-off decision to be made by an engineer, selecting a single point on the Pareto front.

V. Modulation Technique

So far, only SPS modulation and only the full-load operating point at 10 kW was considered. The following section discusses finding an optimized modulation scheme covering the whole operating range. This is done for a single CLLC converter design, i.e., fixed design variables, which are listed in Table II. A schematic of this converter is shown in Fig. 11.

For the CLLC converter, different modulation strategies have been discussed in [28]. In this application, the current-fed property of the secondary side has to be maintained in order to ensure ripple current elimination, therefore the secondary-side duty cycle D_{S} has to remain at 50 %. However, this leaves the following possibilities for influencing the power transfer:

- Varying the phase-shift angle φ (as in SPS modulation)
- Varying the switching frequency f_{sw}
- Varying the primary-side duty cycle D_{P}

Generating a primary-side duty cycle of less than 50 % can either be achieved by modifying the duty cycle of the pri-

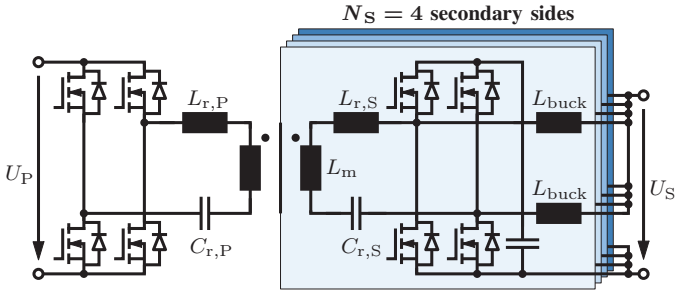

Figure 11: Schematic of the topology for which the modulation techniques are explored

mary-side bridges, or by introducing a phase shift between the two half bridges. The phase-shift solution is preferred here, because it ensures an even loss distribution between the low-side and high-side switches.

The three variables that can be modified to modulate the projected converter can be combined to form seven different possible modulation strategies: Three of them only use one of the variables f_{sw}, D_P, and φ, three of them each use two different variables, and one uses all three variables. For those modulation strategies that modify more than one of the variables, the most efficient variable combination has to be determined for all operating points. For this purpose, another optimization is implemented that takes the modulation variables as design variables and performs multiple single-objective optimizations, one for each operating point, finding the variable combination yielding the least losses. As operating points, the power transfer of 1…10 kW in steps of 500 W is considered, assuming a constant input voltage of 400 V and an output voltage that follows the polarization curve of the electrolyzer at 25 °C as shown in Fig. 1.

Using first harmonic approximation (FHA), the power transfer equation for each of the aforementioned modulation strategies can be approximated as follows [28]:

$$P = \frac{16 \cdot r U_P U_S}{\pi^2 X_r (f_{sw})} \cdot \sin(\pi D_P) \cdot \sin(\varphi), \tag{4}$$

where U_S denotes the electrolyzer stack voltage, r denotes the transformer turns ratio, and X_r denotes the overall impedance of the resonant tank (referred to the primary side) at the switching frequency f_{sw}. A transformer turns ratio of $r = 4$ is assumed, and the secondary-side capacitor voltage is assumed twice the electrolyzer stack voltage due to the 50 % duty cycle on the secondary side. This equation could be used as feed-forward branch for the closed-loop control.

Fig. 12 shows the efficiency of all seven modulation strategies. The highest efficiency is obtained for the modulation strategy that involves all three variables φ, D_P and f_{sw}, since it has the highest degree of freedom. Varying the primary-side duty cycle alone leads to the highest losses due to the large amount of circulating current, whereas all remaining modulation strategies result in efficiency profiles that are close to optimal. However, the optimization procedure does not produce variables that are continuous, therefore any chosen modulation technique has to be probed for its practicality.

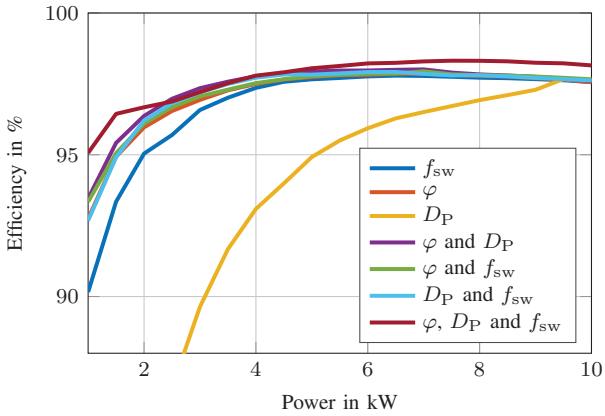

Figure 12: Efficiency curves of the considered modulation strategies

The choice for a modulation strategy, however, does not only depend on the efficiency. If all four secondary sides are used in parallel for powering the electrolyzer, the modulation strategy with the highest efficiency is feasible, where small deviations in the phase-shift angle φ can be used to ensure equal power sharing. If, however, the converter should be adapted to a true multi-port application, e.g., using two secondary sides with the electrolyzer and the other two with a battery storage, resulting in entirely different operating points, the SPS modulation is the most versatile. All in all, however, it has been shown that using FHA and optimization algorithms, also efficiency-optimized modulation strategies can be derived for the projected converter.

VI. Conclusions

This paper addresses a family of current-fed dc-dc converters that supply PEM electrolyzers with a high, ripple-free dc current. Considering a wide range of resonant and non-resonant converter variants, with different configurations of the power stages, different transformer configurations and different degrees of modularity, a genetic optimization algorithm was used to derive the Pareto fronts with respect to efficiency and total stored energy. The results imply critical design decisions: For this application, the CLLC converter is the preferable choice of topology, a full bridge should be used as primary-side circuit, and the secondary side should be modularized as much as possible. Additionally, it has been shown that using FHA and genetic optimization, efficiency-optimized modulation strategies could be derived for the projected converter. Future work could address the simultaneous optimization of the topology and its modulation strategy, the development of a closed-loop control algorithm, and the hardware implementation of the converter.

Acknowledgment

The project “HyInnoLyze” on which this paper is based is funded by the German Federal Ministry of Education and Research under funding code 03ZU1115AB, in the framework of the Hydrogen Clusters4Future. The responsibility for the content of this publication lies with the authors.

REFERENCES

[1] N. Fritz, M. Rashed, and C. Klumpner, "Power density optimization of a dc/dc converter for an aircraft supercapacitors energy storage," in *IEEE International Conference on Electrical Systems for Aircraft, Railway, Ship Propulsion and Road Vehicles & International Transportation Electrification Conference (ESARS-ITEC)*, Nov. 2018.

[2] N. Fritz, M. Rashed, S. Bozhko, F. Cuomo, and P. Wheeler, "Analytical modelling and power density optimisation of a single phase dual active bridge for aircraft application," *The Journal of Engineering*, vol. 2019, no. 17, pp. 3671–3676, 2019.

[3] C. Fronczek, A. Thönnessen, and R. W. De Doncker, "Multi-application multi-objective optimization algorithm for DC-DC converter topology choice," in *IEEE Energy Conversion Congress and Exposition (ECCE)*, Oct. 2022.

[4] N. Fritz, G. Engelmann, A. Stippich, C. Lüdecke, D. A. Philipps, and R. W. De Doncker, "Toward an in-depth understanding of the commutation processes in a SiC MOSFET switching cell including parasitic elements," *IEEE Transactions on Industry Applications*, vol. 56, no. 4, pp. 4089–4101, 2020.

[5] N. Fritz, X. Pan, and R. W. De Doncker, "Speeding up converter design by analytical modeling and genetic optimization – a more electric aircraft example," in *10th IET International Conference on Power Electronics, Machines and Drives (PEMD)*, Dec. 2020.

[6] J. Koponen, V. Ruuskanen, A. Kosonen, M. Niemela, and J. Ahola, "Effect of converter topology on the specific energy consumption of alkaline water electrolyzers," *IEEE Transactions on Power Electronics*, vol. 34, no. 7, pp. 6171–6182, 2019.

[7] J. Koponen *et al.*, "Effect of power quality on the design of proton exchange membrane water electrolysis systems," *Applied Energy*, vol. 279, p. 115 791, 2020.

[8] V. Ruuskanen, J. Koponen, A. Kosonen, M. Niemelä, J. Ahola, and A. Hämäläinen, "Power quality and reactive power of water electrolyzers supplied with thyristor converters," *Journal of Power Sources*, vol. 459, p. 228 075, 2020.

[9] V. Ruuskanen *et al.*, "Power quality estimation of water electrolyzers based on current and voltage measurements," *Journal of Power Sources*, vol. 450, p. 227 603, 2020.

[10] H. P. C. Buitendach, R. Gouws, C. A. Martinson, C. Minnaar, and D. Bessarabov, "Effect of a ripple current on the efficiency of a PEM electrolyser," *Results in Engineering*, vol. 10, p. 100 216, 2021.

[11] F. Parache *et al.*, "Impact of power converter current ripple on the degradation of PEM electrolyzer performances," *Membranes*, vol. 12, no. 2, p. 109, 2022.

[12] J.-H. Kim, M.-H. Jang, J.-S. Choe, D.-Y. Kim, Y.-S. Tak, and B. Cho, "An experimental analysis of the ripple current applied variable frequency characteristic in a polymer electrolyte membrane fuel cell," *Journal of Power Electronics*, vol. 11, 2011.

[13] M. Uno and K. Tanaka, "Pt/c catalyst degradation in proton exchange membrane fuel cells due to high-frequency potential cycling induced by switching power converters," *Journal of Power Sources*, vol. 196, no. 23, pp. 9884–9889, 2011.

[14] H. Xiao, "A modular low current ripple electrolysis power supply based on multiphase half-bridge high-frequency inverters," *IEEE Transactions on Power Electronics*, vol. 35, no. 10, pp. 10 088–10 096, 2020.

[15] D. S. Gautam and A. K. S. Bhat, "A comparison of soft-switched DC-to-DC converters for electrolyzer application," *IEEE Transactions on Power Electronics*, vol. 28, no. 1, pp. 54–63, 2013.

[16] D. Sha, Y. Xu, J. Zhang, and Y. Yan, "Current-fed hybrid dual active bridge DC–DC converter for a fuel cell power conditioning system with reduced input current ripple," *IEEE Transactions on Industrial Electronics*, vol. 64, no. 8, pp. 6628–6638, 2017.

[17] Y. Xiao, Z. Zhang, M. A. E. Andersen, and B. E. Thomsen, "Partial parallel dual active bridge converter with variable voltage gain for SOEC/SOFC system," in *IEEE Applied Power Electronics Conference and Exposition (APEC)*, Mar. 2019.

[18] X. Liu, Z. Wang, and H. Li, "A new fuel cell power conditioning system with extended life time and minimized DC-bus capacitor," in *IEEE Applied Power Electronics Conference and Exposition (APEC)*, Mar. 2013.

[19] X. Sun, Y. Shen, Y. Zhu, and X. Guo, "Interleaved boost-integrated llc resonant converter with fixed-frequency PWM control for renewable energy generation applications," *IEEE Transactions on Power Electronics*, vol. 30, no. 8, pp. 4312–4326, 2015.

[20] X. Pan, H. Li, Y. Liu, T. Zhao, C. Ju, and A. K. Rathore, "An overview and comprehensive comparative evaluation of current-fed-isolated-bidirectional DC/DC converter," *IEEE Transactions on Power Electronics*, vol. 35, no. 3, pp. 2737–2763, 2020.

[21] P. Kowalewski, A. Thönnessen, N. Fritz, and R. W. De Doncker, "A model-based control strategy enhancing the dynamic performance of current-fed triple-active-bridge dc-dc converters," in *2022 IEEE Southern Power Electronics Conference (SPEC)*, 2022.

[22] N. Fritz, D. Heidenberger, C. Fronczek, D. Bündgen, and R. W. De Doncker, "An ultrafast DC-DC converter design methodology combining piecewise linear analytical modelling and genetic algorithms," in *IEEE Workshop on Control and Modeling for Power Electronics (COMPEL)*, Jun. 2022.

[23] G. Tjarks, "PEM-Elektrolyse-Systeme zur Anwendung in Power-to-Gas Anlagen," Dissertation, Forschungszentrum Jülich, 2017.

[24] R. Keller, E. Rauls, M. Hehemann, M. Müller, and M. Carmo, "An adaptive model-based feedforward temperature control of a 100 kW PEM electrolyzer," *Control Engineering Practice*, vol. 120, p. 104 992, 2022.

[25] G. C. Knabben, J. Schafer, L. Peluso, J. W. Kolar, M. J. Kasper, and G. Deboy, "New PCB winding snake-core matrix transformer for ultra-compact wide DC input voltage range hybrid b+DCM resonant server power supply," in *IEEE International Power Electronics and Application Conference and Exposition (PEAC)*, Nov. 2018.

[26] X. Zhou *et al.*, "A high-efficiency high-power-density on-board low-voltage DC–DC converter for electric vehicles application," *IEEE Transactions on Power Electronics*, vol. 36, no. 11, pp. 12 781–12 794, 2021.

[27] L. Tarisciotti, A. Costabeber, L. Chen, A. Walker, and M. Galea, "Current-fed isolated DC/DC converter for future aerospace micro-grids," *IEEE Transactions on Industry Applications*, vol. 55, no. 3, pp. 2823–2832, 2019.

[28] D. Yang, Y. Zhang, X. Liu, W. Wang, and J. Liu, "Overview of CLLC modulation strategy," in *International Power Electronics Conference (IPEC-Himeji 2022 — ECCE Asia)*, May 2022.

[29] J. W. Kolar, J. Biela, S. Waffler, T. Friedli, and U. Badstuebner, "Performance trends and limitations of power electronic systems," in *International Conference on Integrated Power Electronics Systems (CIPS)*, 2010.

[30] TDK Electronics AG. "Epcos product brief 2019: Planar cores for power applications." (Jun. 2019), [Online]. Available: https://www.tdk-electronics.tdk.com/download/2527774/1e429cb7ad3fd0be062bcfe03f8ed498/ferrites-planar-cores-pb.pdf.

[31] J. Sun, L. Yuan, Q. Gu, R. Duan, Z. Lu, and Z. Zhao, "Design-oriented comprehensive time-domain model for CLLC-class isolated bidirectional DC-DC converter for various operation modes," *IEEE Transactions on Power Electronics*, vol. 35, no. 4, pp. 3491–3505, 2020.

[32] K. Venkatachalam, C. Sullivan, T. Abdallah, and H. Tacca, "Accurate prediction of ferrite core loss with nonsinusoidal waveforms using only steinmetz parameters," in *IEEE Workshop on Computers in Power Electronics (CIPE)*, 2002.